

## THE NEARBY NEUTRON STAR RX J0720.4–3125 FROM RADIO TO X-RAYS

D. L. KAPLAN<sup>1</sup>, M. H. VAN KERKWIJK<sup>2</sup>, H. L. MARSHALL<sup>3</sup>, B. A. JACOBY<sup>1</sup>, S. R. KULKARNI<sup>1</sup>  
ANDD. A. FRAIL<sup>4</sup>  
*Accepted by ApJ*

## ABSTRACT

We present radio, optical, ultraviolet, and X-ray observations of the isolated, thermally-emitting neutron star RX J0720.4–3125 using the Parkes radio telescope, the Very Large Array, the *Hubble Space Telescope*, and the *Chandra X-ray Observatory*. From these data we show that the optical/UV spectrum of RX J0720.4–3125 is not well fit by a Rayleigh-Jeans tail as previously thought, but is instead best fit by either a single non-thermal power-law or a combination of a Rayleigh-Jeans tail and a non-thermal power-law. Taken together with the X-ray spectrum, we find the best model for RX J0720.4–3125 to be two blackbodies plus a power-law, with the cool blackbody implying a radius of 11–13 km at an assumed distance of 300 pc. This is similar to many middle aged ( $10^{5-6}$  yr) radio pulsars such as PSR B0656+14, evidence supporting the hypothesis that RX J0720.4–3125 is likely to be an off-beam radio pulsar. The radio data limit the flux at 1.4 GHz to be  $< 0.24$  mJy, or a luminosity limit of  $4\pi d^2 F < 3 \times 10^{25} d_{300}^2$  ergs  $s^{-1}$ , and we see no sign of extended nebulosity, consistent with expectations for a pulsar like RX J0720.4–3125.

*Subject headings:* pulsars: individual (RX J0720.4–3125)—stars: neutron—X-rays: stars

## 1. INTRODUCTION

Thermally-emitting neutron stars have been the targets of many observations recently, as these sources can potentially reveal the equation of state (EOS) of neutron stars, and thereby explore nuclear physics in realms inaccessible from laboratories (Lattimer & Prakash 2000). To obtain the EOS from the spectrum seems simple: determine the effective angular size from spectral fits, multiply by the distance (obtained from other means), and one has the apparent radius. This radius can be converted into the physical radius through use of mass. The radius is the crucial quantity in differentiating between EOS, as most EOS predict a distinctive but small range of radii for a large range of masses. However, in order to use a neutron star to determine the EOS, one needs to (1) be certain that the radiation is from the surface, and (2) have a thorough understanding of this emission. Radio pulsars and accreting binaries are unsuitable since non-thermal magnetospheric emission or emission from the accreting material far exceeds the surface emission.

Therefore the identification of the nearest neutron stars by *ROSAT* was a major advance in the field (see reviews by Motch 2001 and Treves et al. 2000). Most of these sources do not have significant non-thermal emission, so they are prime targets for studies leading to the EOS. The closest of these sources, RX J1856.5–3754, has been the subject of much inquiry lately for just this purpose (e.g., Walter & Lattimer 2002; Drake et al. 2002; Braje & Romani 2002).

RX J0720.4–3125 was discovered by Haberl et al. (1997) as a soft ( $kT \sim 80$  eV), bright X-ray source in the *ROSAT*

All-Sky Survey — the second brightest neutron star that is not a radio pulsar. Given its very low hydrogen column density ( $N_H \sim 1 \times 10^{20}$   $cm^{-2}$ ), nearly sinusoidal 8.39-s pulsations, relatively constant X-ray flux, and very faint ( $B = 26.6$  mag), blue optical counterpart (Kulkarni & van Kerkwijk 1998; Motch & Haberl 1998), it was classified as a nearby, isolated, thermally-emitting neutron star. It is perhaps the second closest source (next to RX J1856.5–3754) that does not show significant non-thermal emission. While originally thought to be an accreting source or possible an old magnetar, recent timing measurements limit the original magnetic field to be smaller than  $10^{14}$  G, eliminating the magnetar hypothesis. However, the discoveries of radio pulsars with periods longer than 4 s (Camilo et al. 2000; Young, Manchester, & Johnston 1999) have led to the suggestion that RX J0720.4–3125 is instead an off-beam radio pulsar, likely with a magnetic field at the high end of the radio-pulsar range ( $B \sim 10^{13}$  G; Kaplan et al. 2002b; Zane et al. 2002).

The spectrum emerging from a thermally-emitting neutron star depends significantly on the composition of the surface (e.g., Romani 1987). In the past, three models have generally been considered. The first, a blackbody, is simple but not physically motivated. Next, light element (H or He, possibly due to accretion from the ISM) atmosphere have few features, all in the (extreme) ultraviolet, and peak, for a given temperature, at a substantially higher energy than a black-body. Finally, heavy element (Fe, Ni) atmospheres peak at a similar location to blackbodies but have many spectral features at a variety of wavelengths.

None of these models can reproduce the X-ray and optical data for RX J0720.4–3125 and RX J1856.5–3754 (Pons et al. 2002; Walter & Lattimer 2002; Drake et al. 2002; Paerels et al. 2001). The X-ray data are well fit by blackbodies, but these blackbodies underpredict the optical flux. The H/He models also match the general shape, but they overpredict the optical flux and the implied radii are larger than is possible for a neutron star. The Fe mod-

<sup>1</sup> Department of Astronomy, 105-24 California Institute of Technology, Pasadena, CA 91125, USA; dlk@astro.caltech.edu

<sup>2</sup> Dept. of Astronomy & Astrophysics, 60 St George St., Toronto, ON, M5S 3H8, Canada

<sup>3</sup> Center for Space Research, Massachusetts Institute of Technology, Cambridge, MA 02139, USA

<sup>4</sup> National Radio Astronomy Observatory, P.O. Box O, Socorro, NM 87801, USA

els have too many lines and edges to match the X-ray spectra. Consequently, the current generation of single-component models have been unsuccessful in fitting both the X-ray and optical fluxes while having radii consistent with those of neutron stars (Pons et al. 2002; Kaplan, van Kerkwijk, & Anderson 2002c). We see, though, how both X-ray and optical data are required to fully constrain the models.

Motivated thus, we present observations of RX J0720.4–3125 from radio to X-ray wavelengths aimed at determining its spectral energy distribution and from that its underlying properties (composition, magnetic field, and geometry). In Section 2 we present new optical/UV data from the *Hubble Space Telescope*, and undertake detailed modeling of the optical/UV spectrum. In Section 3 we present spectroscopic data from the *Chandra X-ray Observatory*, and in Section 4 we present searches for radio sources (both persistent and pulsating) with the Very Large Array and the Parkes radio telescope. Finally, in Section 5 we discuss the spectrum of RX J0720.4–3125, and present our conclusions in Section 6. In the following, all radii refer to the radiation radius as observed at infinity,  $R_\infty$  ( $R_\infty = R_{\text{phys}}/\sqrt{1 - 2GM/R_{\text{phys}}c^2}$ , where  $R_{\text{phys}}$  is the physical radius).

## 2. OPTICAL AND UV DATA

### 2.1. Observations and Analysis

We observed RX J0720.4–3125 with the Space Telescope Imaging Spectrometer (STIS) aboard the *Hubble Space Telescope* (*HST*) four times, covering wavelengths from 125 nm to 900 nm; the observations are summarized in Table 1.

#### 2.1.1. Optical Data

The optical data (50CCD mode) consist of eight unfiltered CCD observations taken in a four-point dither pattern. We assembled the images using the drizzle algorithm (Fruchter & Hook 2002) giving a plate-scale of  $25.3 \text{ mas pixel}^{-1}$ . We show the stacked image in Figure 1.

We performed standard aperture photometry on the stacked STIS image using IRAF’s *daophot* package. The sky level was estimated using an annulus from  $0''.75$ – $1''.00$ . The source flux was measured within an aperture of radius  $0''.5$ . While there were no aperture corrections strictly appropriate for a source with the color of RX J0720.4–3125 ( $B - V \approx -0.3 \text{ mag}$ ), we used the bluest of the color-dependent aperture corrections available (T. Brown 2002, personal communication) to correct the flux to an infinite aperture. We estimate that the aperture correction introduces an uncertainty of  $< 0.02 \text{ mag}$ , as blue sources like RX J0720.4–3125 have less scattered light than redder sources and therefore the aperture corrections are better determined (see Kaplan et al. 2002a). Given the very wide 50CCD bandpass (FWHM  $\approx 441 \text{ nm}$ ) a single zero-point flux is not appropriate for all source spectra. Therefore, as a first order estimate, we calculated the zero-point flux at the mean wavelength of the filter (given in Table 1), assuming an input spectrum with  $F_\lambda \propto \lambda^{-4}$  and  $A_V \approx 0.1 \text{ mag}$ , appropriate for RX J0720.4–3125 (Kulkarni & van Kerkwijk 1998).

For astrometric purposes we used 10-s and 60-min R-band images taken with the Low-Resolution Imaging Spec-

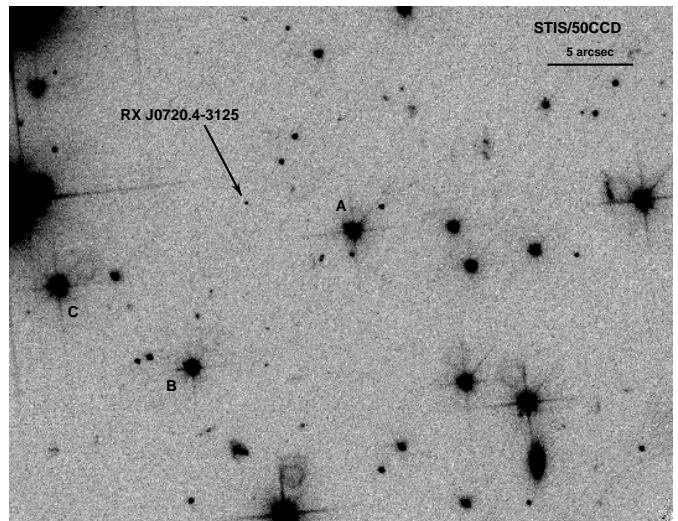


FIG. 1.— STIS optical image of RX J0720.4–3125. North is up, East to the left. The scale bar in the upper right indicates  $5''$ . RX J0720.4–3125 is indicated by the arrow, and sources A, B, and C from Haberl et al. (1997) are also marked.

trograph (Oke et al. 1995) on the 10-m Keck I telescope (the observations are described in Kulkarni & van Kerkwijk 1998). We determined the centroids of 231 stars from the Guide Star Catalog version 2.2 (GSC-2.2) on the 10-s image, rejecting 50 objects that were overexposed or appeared to be incorrectly identified. The pixel coordinates were corrected for instrumental distortion using a cubic radial distortion function<sup>5</sup>, and we then fit for the zero-point position, rotation, and plate-scale of the image. The rms was  $0''.12$  in each coordinate. We then fit the 70 non-saturated stars from the 10-s image to the 60-min composite image, again correcting for instrumental distortion. This fit had rms of  $0''.024$  in each coordinate. Finally, we performed a fit using 25 stars from the 60-min image to determine the zero-point, scale, and rotation of the STIS image (which had been corrected for distortion during the drizzle process), giving an rms of  $0''.025$  in each coordinate. Overall, the STIS image is tied to the frame of the GSC-2.2 with uncertainty of  $0''.01$  in each coordinate, or tied to the International Coordinate Reference Frame (ICRF) with uncertainty of about  $0''.2$  in each coordinate. The final position for RX J0720.4–3125 is (J2000, epoch MJD 52106)  $\alpha = 07^{\text{h}}20^{\text{m}}24^{\text{s}}.961$ ,  $\delta = -31^{\circ}25'50''.21$ . This supersedes the position of Kulkarni & van Kerkwijk (1998), as the significance of the new detection is far higher and the position is directly tied to the ICRF. The *HST* position is consistent with the X-ray position which has uncertainties of  $\approx 0''.6$  in each coordinate (Kaplan et al. 2002b).

#### 2.1.2. UV Data

For the UV MAMA data, we corrected the arrival times of the data to the Solar System barycenter using the *stsdas* task *odelaytime*. We then filtered the photon lists for the FUV data for periods of high background. These occurred at the beginning of each orbit as *HST* was going into the Earth’s shadow. Using a background annulus from  $3''.0$ – $3''.5$ , we estimated the median background level from a light-curve binned to 50-s and only used the data

<sup>5</sup> See <http://alamosana.keck.hawaii.edu/inst/lris/coordinates.html>.

TABLE 1  
SUMMARY OF STIS OBSERVATIONS

Detector/Filter	Date (UT)	Exposure (sec)	$\langle \lambda \rangle^a$ (Å)	$\langle A_\lambda / A_V \rangle^a$ (mag)	Ap. Corr. <sup>b</sup> (mag)	$\Delta Z_{\text{mag}}^c$ (mag)	Magnitude <sup>d</sup> (mag)
Calculated for $\alpha_\nu = 2.00$ and $A_0 = 0.13$ mag. <sup>e</sup>							
CCD/50CCD	2001-Jul-16	5342	5148	1.56	0.102	...	$26.68 \pm 0.10$
NUV MAMA/25Qtz	2001-Aug-05	5500	2286	2.58	0.276	0.029	$23.82 \pm 0.14$
FUV MAMA/25SrF <sub>2</sub>	2002-Jan-28	4800	1447	2.80	0.340	0.087	$21.97 \pm 0.11$
FUV MAMA/25MAMA	2002-Feb-13	3850	1360	2.97	0.353	0.078	$21.6 \pm 0.2$
Calculated for $\alpha_\nu = 1.40$ and $A_0 = 0.10$ mag. <sup>f</sup>							
CCD/50CCD	...	...	5367	1.41	0.102	...	$26.68 \pm 0.10$
NUV MAMA/25Qtz	...	...	2310	2.56	0.270	0.029	$23.83 \pm 0.14$
FUV MAMA/25SrF <sub>2</sub>	...	...	1450	2.79	0.339	0.088	$21.96 \pm 0.11$
FUV MAMA/25MAMA	...	...	1365	2.95	0.352	0.079	$21.7 \pm 0.2$

<sup>a</sup>Effective wavelength and normalized extinction; see Appendix A of van Kerkwijk & Kulkarni (2001b).

<sup>b</sup>Aperture correction from a radius of  $0''.5$  to infinity. See § 2 for details.

<sup>c</sup>Change in the zero-point magnitude due to degradation of the MAMA detectors.

<sup>d</sup>Magnitude in the STMAG system, with  $m_{\text{ST}} = -21.1 - 2.5 \log_{10} F_\lambda$ , corrected to infinite aperture.

<sup>e</sup>Appropriate for the RJ fit in Table 4.

<sup>f</sup>Appropriate for all fits except the RJ fit in Table 4.

NOTE.—All filter curves were taken from the `synphot` database.  $\lambda_0 = 4500$  Å.

where the background level was within  $\pm 3\sigma$  of the median. We found that the background was noticeably high only for the FUV MAMA/25SrF<sub>2</sub> data, where we have retained 4800 s of the original 5500 s.

We then performed aperture photometry on the raw photon data. The source flux was computed using a radius of  $0''.5$ , where the signal-to-noise was relatively high and the aperture corrections were well-defined. The raw source and background counts are given in Table 2. The STIS MAMAs have wide point-spread-functions (psfs), with substantial flux beyond  $0''.5$ , and therefore aperture corrections are particularly important. We took the monochromatic aperture corrections for the MAMAs (T. Brown 2002, personal communication) convolved with the expected source spectrum and the filter throughputs to compute aperture corrections for each filter, which we give in Table 1. Another issue with the STIS MAMAs is that the sensitivity changes with time (Stys et al. 2002) at the level of a few percent per year. Using a wavelength-dependent fit to the sensitivity changes (D. Stys 2002, personal communication; R. Diaz-Miller 2002, personal communication; these corrections are now incorporated into the STIS pipeline), we computed weighted zero-point corrections for the NUV and FUV MAMA data that are listed in Table 1. These corrections were small, less than 0.1 mag. As with the optical data, the zero-point fluxes were calculated at the mean wavelengths of the filters.

The STIS MAMA data are time-tagged with 125  $\mu\text{s}$  resolution, but we could not detect the 8.39-s periodicity present in the X-rays. We find 90% confidence upper limits on the Fourier power (normalized to have unity mean

and rms) present at the X-ray period (given by Kaplan et al. 2002b) of 5.3 and 5.9, for the NUV and FUV/SrF<sub>2</sub> data sets, respectively. These translate into limits on the rms pulsed fraction of 0.16 and 0.19, respectively.

## 2.2. Spectral Fits

### 2.2.1. Power-law Fits

We already know from Kulkarni & van Kerkwijk (1998) that the optical spectrum of RX J0720.4–3125 is roughly approximated by the Rayleigh-Jeans portion of a black-body curve:  $F_\lambda \propto \lambda^{-4}$ . We can now investigate this more quantitatively and over a wider range of wavelengths. Here we use the optical and UV data presented in this paper as well as the *B* and *R* photometry from Kulkarni & van Kerkwijk (1998); for the data from Kulkarni & van Kerkwijk (1998), we used the zero-point fluxes from Bessell, Castelli, & Plez (1998).

Our spectral fitting followed van Kerkwijk & Kulkarni (2001b). We fit the data with a sum of extinguished power-law (PL) of the form

$$F_\lambda = F_0 \left( \frac{\lambda}{\lambda_0} \right)^{-(2+\alpha_\nu)} 10^{-A_0 A'_\lambda / 2.5}, \quad (1)$$

where  $\alpha_\nu$  is the spectral index<sup>6</sup>,  $F_0$  is the observed flux at the reference wavelength  $\lambda_0$ ,  $A_0$  is the extinction at  $\lambda_0$ , and  $A'_\lambda$  is the normalized extinction at wavelength  $\lambda$  ( $A'_\lambda \equiv A_\lambda / A_0$ ). We use the reddening curve of Cardelli, Clayton, & Mathis (1989), with corrections to the optical and UV portions from O'Donnell (1994). We chose  $\lambda_0 =$

<sup>6</sup> From this definition we also have the more standard  $F_\nu \propto \nu^{\alpha_\nu}$ .

TABLE 2  
SOURCE AND BACKGROUND COUNTS FOR STIS UV DATA

Detector/Filter	Counts	
	Source	Background
NUV MAMA/25Qtz	$3534 \pm 59$	$2788 \pm 15$
FUV MAMA/25SrF <sub>2</sub>	$611 \pm 25$	$128 \pm 3$
FUV MAMA/25MAMA	$14502 \pm 120$	$13788 \pm 58$

NOTE.—No aperture corrections have been applied. Background counts are normalized to the same area as the source counts.

4500 Å ( $A_0 = 1.29A_V$ , or  $A_0 \approx A_B$ ), as this is the mean wavelength of the data.

For the fit, we calculated likelihood values as we varied  $F_0$ ,  $A_0$ , and  $\alpha_\nu$ . However, as the spectral shape changes (i.e. variations in  $A_0$  and  $\alpha_\nu$ ) the aperture corrections, reference wavelengths, extinctions, and zero-point corrections (from Table 1) also change (these changes are most significant for the STIS/50CCD data). Therefore, during the iterations of the fitting, we recomputed all of the spectrum-dependent quantities for each combination of  $A_0$  and  $\alpha_\nu$ .

The results of the fitting for the two basic models — Rayleigh-Jeans<sup>7</sup> (RJ) and unconstrained power-law (PL) are given in Table 3. These fits give values of the extinction  $A_0 \sim 0.5$  mag. This is much higher than expected from other observations. From the X-ray spectrum of RX J0720.4–3125, we know that the hydrogen column density is  $N_H \approx 1.3 \times 10^{20} \text{ cm}^{-2}$ , which implies  $A_V \approx 0.07$  mag (Predehl & Schmitt 1995) or  $A_0 \approx 0.09$  mag. Kulkarni & van Kerkwijk (1998) have placed an upper limit on the reddening of  $E_{B-V} < 0.04$ , as RX J0720.4–3125 is in the foreground of the open cluster Collinder 140, which implies  $A_0 < 0.10$  (for the standard ratio of  $R_V = 3.2$ ). We therefore expect small values of the extinction:  $A_0 \lesssim 0.15$  mag, allowing for uncertainties in  $N_H$ ,  $R_V$ , and the relation between  $N_H$  and  $A_V$ . From this we can reject the models in Table 3.

Therefore we constrained  $A_0$  from the information above. To formally include this in our fit, we performed a maximum likelihood fit with the following prior distribution for  $A_0$ :

$$f_{A_0}(A_0) = \mathcal{N}_6(A_0|0.09 \text{ mag}, 0.06 \text{ mag}), \quad (2)$$

where  $\mathcal{N}_n(x|\mu, \sigma)$  is a generalized Gaussian distribution of degree  $n$  ( $n$  is even) with the form:

$$\mathcal{N}_n(x|\mu, \sigma) \equiv \frac{n}{2\sqrt{2}\pi\sigma} \Gamma\left(\frac{n-1}{n}\right) \sin\left(\frac{\pi}{n}\right) \times \exp\left[-\left(\frac{(x-\mu)}{\sqrt{2}\sigma}\right)^n\right]. \quad (3)$$

For  $n = 6$ , this distribution essentially requires that  $A_0$  be between 0 mag and 0.18 mag. We could have used a

<sup>7</sup> For blackbodies of the temperatures considered here, the Rayleigh-Jeans approximation holds at the shortest UV wavelength used to better than 4% — considerably smaller than the measurement error.

uniform prior with  $A_0 = 0-0.15$  mag, but the sharp edges of this distribution can make for discontinuities in the resulting posterior distributions, so we opted for Equation 2, which is a smoothed version of the uniform distribution.

We consider four power-law models for the fit. The first, given in the PL column in Table 4, is a single power-law fit to the optical/UV data alone. The second, given in the RJ column in Table 4, is a single power-law fit to the optical/UV data, but where the power-law index is that of a Rayleigh-Jeans tail ( $\alpha_\nu = 2$ ). The third is a fit where there are two power-laws, given in the PL+RJ column in Table 4: one has an unconstrained index, and the other has  $\alpha_\nu = 2$ . Finally, the fourth fit, given in the PL+X-ray column in Table 4, has a Rayleigh-Jeans power-law present, but its normalization is set by the X-ray fit (§ 3; the uncertainties in the X-ray flux extrapolated to optical/UV wavelengths is  $\approx 10\%$ ).

In Tables 3 and 4 we give  $\chi^2$  values for each fit. These values were computed from the data without taking into account the prior distributions used in Table 4. The best-

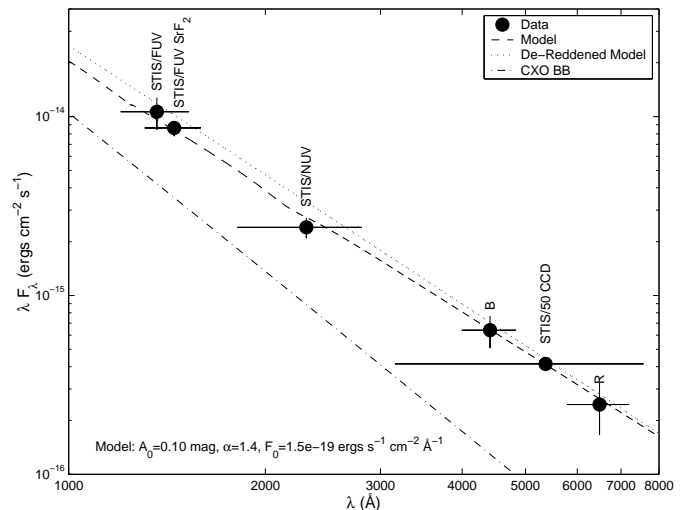


FIG. 2.— Optical/UV spectrum of RX J0720.4–3125, with data from Kulkarni & van Kerkwijk (1998) and this paper. The PL fit is shown, with: the best-fit model (dashed line), the best-fit model corrected for extinction (dotted line) and the extrapolation of the *Chandra* blackbody fit (dash-dotted line; “CXO BB”; see § 3). The different bands are labeled.

TABLE 3  
 FITS TO RX J0720.4–3125 OPTICAL/UV DATA WITH  $A_0$  UNCONSTRAINED

Parameter	Type of Fit	
	PL	RJ
$A_0$ (mag)	0.47(15)	0.59(6)
$\alpha_\nu$ <sup>a</sup>	1.9(2)	2
$F_0$ ( $\times 10^{-19}$ ergs s <sup>-1</sup> cm <sup>-2</sup> Å <sup>-1</sup> )	2.5(6)	3.0(3)
$B_0$ (mag) <sup>b</sup>	26.0(2)	25.82(10)
$\chi^2$	1.0	1.1
DOF	3	4
$\chi^2$ /DOF	0.3	0.3

<sup>a</sup>The spectral index such that  $F_\lambda \propto \lambda^{-(2+\alpha_\nu)}$ .

<sup>b</sup> $B$ -band Vega-magnitude corresponding to  $F_0$ .

NOTE.—Numbers in parentheses are 68% confidence limits in the last digit(s). Values without confidence limits were held fixed for the fit. Values with subscript 0 are for  $\lambda_0 = 4500$  Å.

TABLE 4  
 FITS TO RX J0720.4–3125 OPTICAL/UV DATA WITH  $A_0$  CONSTRAINED

Parameter	Type of Fit			
	PL	RJ	PL+RJ	PL+X-ray
$A_0$ (mag)	0.10(6)	0.19(2)	0.10(4)	0.09(4)
$\alpha_\nu$ <sup>a</sup>	1.40(4)	2	0.3(7)	1.14(12)
$F_0$ ( $\times 10^{-19}$ ergs s <sup>-1</sup> cm <sup>-2</sup> Å <sup>-1</sup> )	1.50(12)	1.12(7)	0.8(2)	1.24(9)
$B_0$ (mag) <sup>b</sup>	26.58(8)	26.88(7)	27.4(2)	26.79(8)
$\alpha_{\nu,2}$ <sup>a</sup>	...	...	2	2
$F_{0,2}$ ( $\times 10^{-19}$ ergs s <sup>-1</sup> cm <sup>-2</sup> Å <sup>-1</sup> )	...	...	0.6(2)	0.27
$B_{0,2}$ (mag) <sup>b</sup>	...	...	27.5(3)	28.5
$\chi^2$ <sup>c</sup>	1.9	26.5	0.8	1.4
DOF	3	4	2	3
$\chi^2$ /DOF	0.6	6.6	0.4	0.5

<sup>a</sup>The spectral index such that  $F_\lambda \propto \lambda^{-(2+\alpha_\nu)}$ .

<sup>b</sup> $B$ -band Vega-magnitude corresponding to  $F_0$ .

<sup>c</sup>The  $\chi^2$  values are raw values that do not take into account the prior distributions (e.g., Eqn. 2). They are there only as a guide, showing which models do and do not fit the data independent of the prior distributions.

NOTE.—Numbers in parentheses are 68% confidence limits in the last digit(s). Values without confidence limits were held fixed for the fit. Values with subscript 0 are for  $\lambda_0 = 4500$  Å.  $A_0$  was constrained by use of Equation 2.

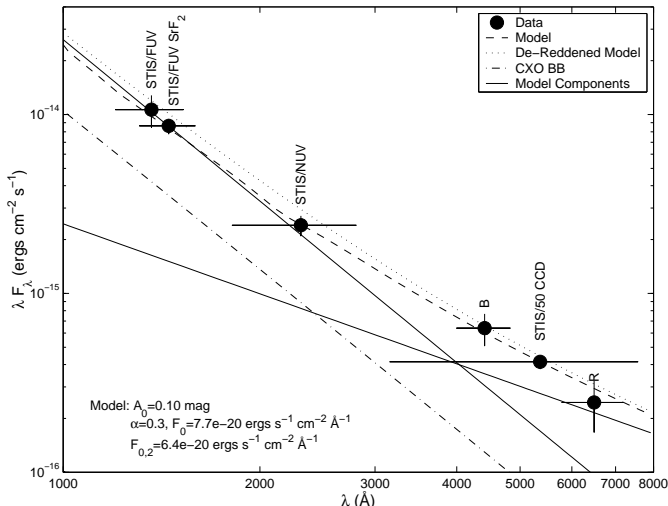


FIG. 3.— Optical/UV spectrum of RX J0720.4–3125, with data from Kulkarni & van Kerkwijk (1998) and this paper. The PL+RJ fit (unconstrained Rayleigh-Jeans tail plus a second PL) is shown: the best-fit model (dashed line), the best-fit model corrected for extinction (dotted line), the two components of the model (solid lines), and the extrapolation of the *Chandra* blackbody fit (dash-dotted line; “CXO BB”; see § 3). The different bands are labeled.

fit values of the parameters were computed not by using the  $\chi^2$  values themselves but through the marginalized likelihood functions that incorporated the prior. The  $\chi^2$  values are there only as a reference, to show that even with the prior distribution in place the fits are still good. One should not use the typical  $\Delta\chi^2$  technique (Press et al. 1992, p. 697) for determining parameter uncertainties — while the PL models from Tables 3 and 4 have  $\chi^2$ ’s that differ by 0.9, the PL model from Table 3 is excluded very significantly by the fit in Table 4, as shown by the small uncertainties in the parameters of Table 4. Instead the confidence limits given in Tables 3 and 4 are single-parameter 68% limits determined from the marginalized likelihood functions.

We find a good fit for the single unconstrained power-law, shown in Figure 2. This model has  $\chi^2 = 1.9$  for 3 degrees-of-freedom (DOF). The Rayleigh-Jeans fit, though, is significantly worse, with  $\chi^2 = 26.5$  for 4 degrees of freedom under the same prior assumptions. We can therefore reject  $\alpha_\nu = 2$  with  $> 98\%$  confidence. For the PL+RJ fit, the results are given in the PL+RJ column of Table 4. The fit, shown in Figure 3, is good, with  $\chi^2 = 0.8$  for 2 DOF. For the final fit, PL+X-ray, we also find an acceptable value of  $\chi^2 = 1.4$  for 3 DOF. We can conclude that all of the fits except the RJ fit are acceptable.

As mentioned above, the values of  $\langle\lambda\rangle$ ,  $A'_\lambda$ , the aperture correction and the zero-point correction change depending on the spectral model. However, except for the RJ fit, all of the models have sufficiently similar flux distributions, despite the different contributions from different components, that the values are essentially the same for these models. We give the values of these parameters for the best-fit values of  $\alpha_\nu$  and  $A_0$  in Table 1; these will apply to the PL, PL+RJ, and PL+X-ray models. The only filter whose calibration changes significantly is the extremely broad-band STIS/50CCD.

As seen in Figure 2, the PL fit has a shallower slope than the extrapolation of the *Chandra* blackbody spectrum. While an extrapolation of the optical/UV PL does not intersect the X-ray spectrum, it does come to within a factor of 1.2 (at 142 Å). By the lower energy end of the *Chandra* data (0.1 keV  $\approx$  125 Å), the optical/UV PL must have turned over as it is not seen in the X-rays. The power-law component of the PL+X-ray fit behaves similarly.

The best-fit Rayleigh-Jeans component of the PL+RJ model is a factor of 2.4(4) above the extrapolation of the X-ray blackbody (Fig. 3 and Tab. 4). The two components contribute equally at  $\lambda = 4930$  Å: at shorter wavelengths the Rayleigh-Jeans component dominates, while at longer wavelengths the non-thermal component dominates. The non-thermal PL component is above the X-ray extrapolation in the optical regime, intersects it at 2680 Å, and the continues below it. Therefore, the non-thermal PL would not be seen in soft X-rays or in the radio (Fig. 4), although it may approach the X-ray spectrum at energies  $\gtrsim 2$  keV.

### 2.2.2. Disk Fits

We also considered fits to the optical/UV data that include a disk of accreting material, such as that proposed to account for the X-ray luminosity and periodicity of RX J0720.4–3125 (e.g., Wang 1997; Konenkov & Popov 1997; Alpar 2001). For the disk spectrum we used the model of Perna, Hernquist, & Narayan (2000). We found fits using a disk model to be unsatisfactory. As there are too many free parameters to do a formal fit (the inner and outer disk radii, the disk inclination, as well as two undetermined efficiency factors), we varied subsets of the

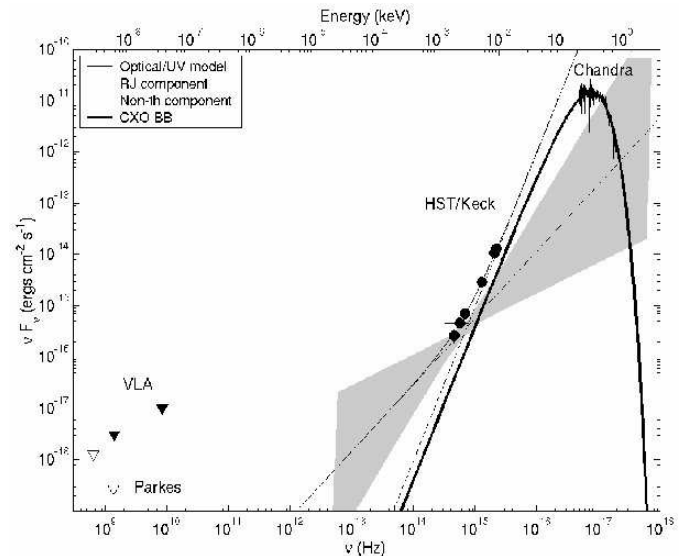


FIG. 4.— Broad-band spectrum of RX J0720.4–3125, from radio to X-rays. The absorption-corrected optical/UV data (§ 2) are plotted as filled circles, the absorption-corrected X-ray data (§ 3) as points, the VLA upper limits (§ 4.1) as filled triangles, and the Parkes upper limits for pulse widths of 0.6–3% (§ 4.2) as the open triangles. The models are: X-ray blackbody (thick solid line), Rayleigh-Jeans component of the PL+RJ fit to the optical/UV data (dashed line), non-thermal component of the PL+RJ fit (dash-dotted line), and the overall PL+RJ fit to the optical/UV data (thin solid line). The  $\pm 1\sigma$  uncertainties on the non-thermal PL are shown by the shaded region.

parameters by hand. We first considered disks that extend in to the corotation radius and out to infinity. For most conceivable disk inclinations ( $i \lesssim 85^\circ$ ) the disk alone is a factor of 10–20 above the optical data, and this is without any contribution to the optical emission from the neutron star surface. Toward the short-wavelength end of the disk, where the emission decreases below the level of our data and the contribution is primarily from the inner edge of the disk, the slope is entirely inconsistent with the optical/UV data: it goes approximately as  $F_\lambda \propto \lambda^4$ , while the excess flux in the optical (compared to a Rayleigh-Jeans tail) is like  $F_\lambda \propto \lambda^{-2.3}$ . We therefore consider this disk model to be very unlikely for RX J0720.4–3125.

There are disk models that can reproduce a spectrum roughly similar to that observed. This occurs when the inner radius is far inside the corotation radius and approaches the neutron star surface, while the outer radius move inward to  $\sim 10^8$  cm. But while the spectral shapes are not inconsistent, the flux predicted by such disks is a factor of  $\sim 100$  above the optical/UV data. Also, there is no natural reason for the disk to be truncated at such small radii (the optical data do not allow for any stellar companion). Therefore this disk model is also very unlikely for RX J0720.4–3125.

### 2.2.3. Variability

It is possible that the spectrum of RX J0720.4–3125 is a Rayleigh-Jeans tail in the optical, and that the deviations we see are temporal in nature: i.e. RX J0720.4–3125 could vary. However, we consider this unlikely. First, the X-ray flux has been extremely constant over almost a decade of observation (Haberl et al. 1997; Paerels et al. 2001). Second, similar sources such as RX J1856.5–3754 and PSR B0656+14 have exhibited constant optical fluxes, again over several years of observations (van Kerkwijk & Kulkarni 2001b; Koptsevich et al. 2001).

Regardless, we can perform a simple test for variability. We have an ongoing series of *HST* observations that, while designed to measure the parallax and proper motion of RX J0720.4–3125, also provide a sensitive flux monitor. Only the first two epochs of data have been observed so far (at MJDs 52459 and 52532). The data are from 4950-s observations with the Advanced Camera for Surveys on *HST* using the High Resolution Camera (ACS/HRC) in the F475W filter. The photometric calibration of ACS is not complete, so we cannot directly compare the measured flux of RX J0720.4–3125 to the models presented here (although the new data are roughly consistent), but we can look for variations in the flux of RX J0720.4–3125 and in that of the other sources in the field. We drizzled the data using a preliminary model of the ACS/HRC geometric distortion, and then performed aperture photometry on RX J0720.4–3125 and 11 other sources, ranging from much brighter than RX J0720.4–3125 to about as bright as RX J0720.4–3125. The field sources changed by  $0.02 \pm 0.04$  mag from the first epoch to the second, while RX J0720.4–3125 changed by  $-0.10 \pm 0.09$  mag. This number is preliminary, but shows that the flux of RX J0720.4–3125 changed by at most 10% over two months. We will eventually have better-calibrated data spanning two years, which will allow us to make a much more rigorous test for variability.

## 3. X-RAY DATA

RX J0720.4–3125 was observed with the *Chandra X-ray Observatory*, using the High Resolution Camera spectroscopic detector (HRC-S) with the Low Energy Transmission Grating (LETG); the observations are summarized in Table 5. Here we describe the spectroscopic analysis of these data — timing analysis is described in Kaplan et al. (2002b) and Zane et al. (2002).

The spectral data were reduced from standard event lists using IDL using custom processing scripts as described in Marshall & Schulz (2002) and Marshall et al. (2002). Raw events were extracted from first and higher orders and calibrated with an updated model of the LETGS effective area<sup>8</sup> (EA), which was developed from observations of PKS 2155–304.

Integrating the observed fluxes over the 0.25–3.0 keV band gives an observed flux of  $(9 \pm 2) \times 10^{-12}$  ergs cm<sup>-2</sup> s<sup>-1</sup> and an absorbed luminosity of  $(9 \pm 2) \times 10^{31} d_{300}^2$  ergs s<sup>-1</sup>, where  $d = 300 d_{300}$  pc is the distance to RX J0720.4–3125 (Kaplan et al. 2002c). The data were rebinned adaptively to provide a signal-to-noise ratio (S/N) of 5 in each bin over the 0.10–2.0 keV range. The spectrum, shown in Figure 5, was first estimated using the first-order EA only. The contributions to the observed counts from high orders are estimated by folding a model for first-order through the high-order EA (important only below 0.2 keV).

Following previous analyses (Haberl et al. 1997; Paerels et al. 2001), we modeled the continuum by an absorbed blackbody; the fitted parameters are given in Table 6. We exclude the data below 0.15 keV from the fit where uncertainties in the high-order grating efficiencies can be important. This fit gives a temperature of 81.4(13) eV and a bolometric luminosity of  $2.1 \times 10^{32} d_{300}^2$  ergs s<sup>-1</sup>, consistent with the *ROSAT* and *XMM* analyses (Haberl et al. 1997; Paerels et al. 2001), given the uncertainties in mod-

<sup>8</sup> This effective area is available at [http://cxc.harvard.edu/cal/Links/Letg/User/Hrc\\_QE/EA/correct\\_ea/letgs\\_NOGAP\\_EA\\_001031.mod](http://cxc.harvard.edu/cal/Links/Letg/User/Hrc_QE/EA/correct_ea/letgs_NOGAP_EA_001031.mod).

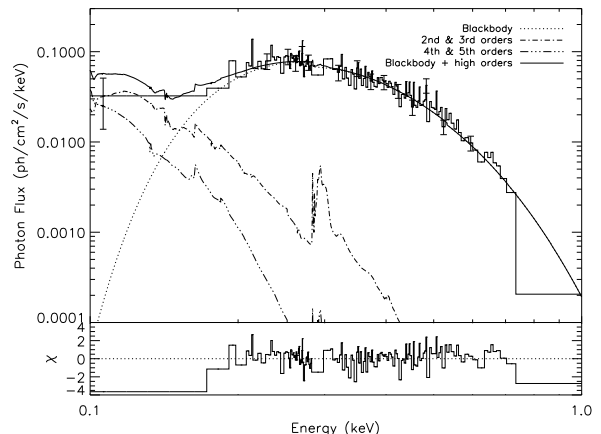


FIG. 5.— LETGS spectrum of RX J0720.4–3125. The bin sizes have been varied to provide good signals in each energy bin; the uncertainties are about 20% everywhere. Solid line: Model consisting of one blackbody component. High orders do not contribute significantly for  $E > 0.20$  keV, while the data at low energies ( $E < 0.15$  keV) are best modeled as the result of the sum of high orders.

TABLE 5  
SUMMARY OF *Chandra* HRC-S/LETG OBSERVATIONS

Date (UT)	Exposure (ksec)	Counts	
		Order 0	Orders $\pm 1$
2000-Feb-01	5.4	929	671
2000-Feb-02	26.3	4584	3027
2000-Feb-04	6.1	1119	687

TABLE 6  
ONE AND TWO BLACKBODY FIT TO THE LETG SPECTRUM

Parameter	Value	
$N_H$ ( $\times 10^{20}$ cm $^{-2}$ )	1.32(14)	1.46(14)
$T_{\text{hot}}$ ( $\times 10^5$ K)	9.45(15)	9.47(15)
$R_{\text{hot}}$ (km)	6.1(3) $d_{300}$	6.1(6) $d_{300}$
$T_{\text{cold}}$ ( $\times 10^5$ K)	...	3.72(10)
$R_{\text{cold}}$ (km)	...	15(17)
$\chi^2$	163.9	163.1
DOF	148	146
$\chi^2/\text{DOF}$	1.11	1.12

NOTE.—Numbers in parentheses are 68% confidence limits in the last digit(s).

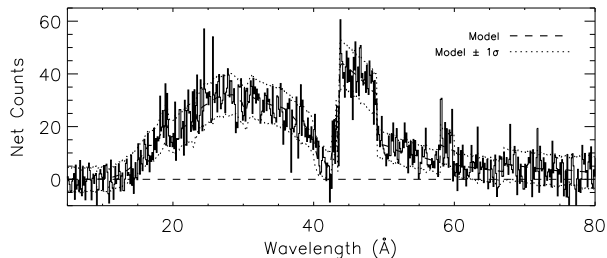


FIG. 6.— Count spectrum of RX J0720.4–3125 obtained with the LETGS. A binning of 0.125 Å was used to obtain sufficient signals per bin to search for narrow features. Heavy dashed line: Expected count spectrum from the single blackbody model shown in Fig. 5. Light dotted lines:  $\pm 1\sigma$  uncertainties about the model. The residuals are consistent with statistical fluctuations about the model. The sharp edges in the model near the 50–70 Å range are the result of detector gaps.

eling the effective areas below 0.2 keV and the higher order responses. The fit has a reduced  $\chi^2 = 1.11$  (for 148 DOF), acceptable at the 90% level. Other models, such as those with non-thermal power-laws or a second blackbody, did not improve the fit.

The best-fit model is plotted against the fitted data in Figure 5. The count spectrum (Fig. 6) was binned at 0.125 Å resolution in order to search for narrow spectral features against the continuum model. No significant emission or absorption features were found: in Figure 7 we give  $3\sigma$  upper limits to the equivalent width of narrow-line features in our data. The *Chandra* data are generally consis-

tent with the *XMM* data (Paerels et al. 2001), although now the upper limit for the energy of any narrow features is somewhat lower, around 0.2 keV.

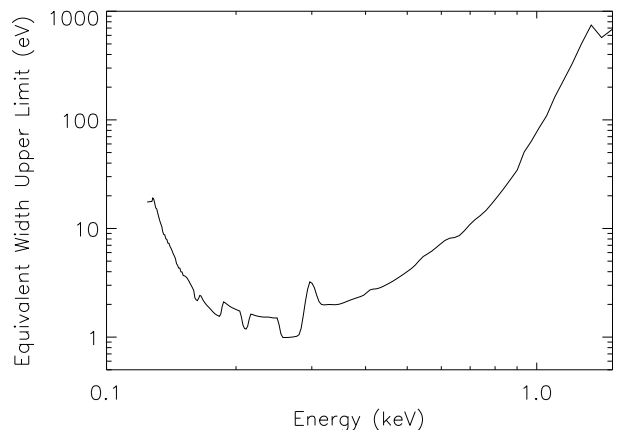


FIG. 7.— Estimates of the  $3\sigma$  limits that can be placed on any emission lines whose FWHMs are comparable to the instrument resolution, as a function of energy. The computation uses the model fitted to the data (Fig. 5) and the effective areas. We assume that candidate features are only 2 bins (0.25 Å) wide. The curves are rather smooth, except for locations of chip gaps, so one may derive limits on broad features using these curves until the scale of the feature becomes comparable to that of the instrument calibration uncertainties. Limits on absorption features are identical when there are many counts but are systematically larger at the high and low ends of the spectrum, where there are fewer than 25 counts per bin.



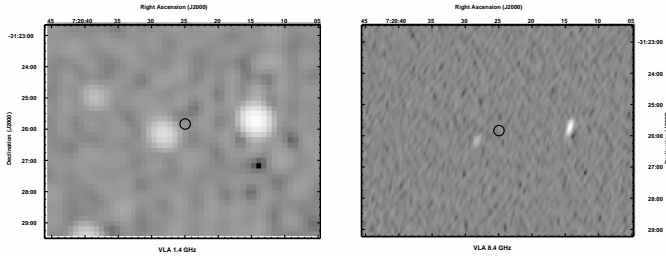


FIG. 8.— VLA maps of the field around RX J0720.4–3125. Left: 1.4 GHz map from the 1999 observations. Right: 8.4 GHz map. RX J0720.4–3125 is indicated with the circle at the center (the radius of the circle is  $10''$ ).

## 4. RADIO OBSERVATIONS

### 4.1. Synthesis Imaging

We observed RX J0720.4–3125 with the Very Large Array (VLA) once at 8.4 GHz and twice at 1.4 GHz (summarized in Table 7) in the standard synthesis-imaging mode. All data sets were independently calibrated using AIPS, but the two 1.4 GHz observations were combined for imaging.

For the 1.4 GHz data, we performed imaging and self-calibration in `difmap`. We iteratively cleaned and self-calibrated (phase only) until the gain solution converged. Uniform weighting was used, yielding a synthesized beam with  $\text{FWHM} \approx 34''$ . An overall gain adjustment was added for one IF, effectively correcting for a non-zero spectral index across the two IF's. No additional amplitude self-calibration was necessary.

After cleaning, we found rms map noise to be 0.08 mJy, a factor of  $\sim 8$  higher than the theoretical thermal noise but consistent with confusion (Condon et al. 1998). The final image (see Fig. 8) shows a 5.0 mJy point source next to the position of RX J0720.4–3125, but we believe that this source is unrelated. For reference, the radio source is at J2000  $\alpha = 07^{\text{h}}20^{\text{m}}28^{\text{s}}.28(2)$ ,  $\delta = -31^{\circ}26'09''.9(3)$ ,  $46''$  away from the nominal position of the source. No point-like or diffuse emission from RX J0720.4–3125 was found, which then gives  $3\sigma$  upper limits to the flux of a point-source of 0.24 mJy and to that of an extended source of  $< 0.43 \text{ mJy arcmin}^{-2}$ .

The imaging of the 8.4 GHz data proceeded similarly. Cleaning and phase self-calibration were done in `difmap`. Again, no source was found at the position of RX J0720.4–3125 (see Fig. 8), giving a  $3\sigma$  flux limit of 0.12 mJy.

### 4.2. Pulsation Searches

We observed RX J0720–3125 with the 64-m Parkes radio telescope on 11 January 2001 in an attempt to detect pulsed radio emission. The target position was observed for 10,800 s at center frequencies of 1374 MHz and 644 MHz. At the higher frequency we used the center beam of the Parkes multibeam receiver to feed a  $3 \text{ MHz} \times 96$ -channel multibeam filterbank (see Lyne et al. 2000). At 644 MHz the front-end was the Parkes 50-cm receiver, and the back-end was a  $0.125 \text{ MHz} \times 256$ -channel filterbank. Both observations employed a 1-ms sample period and one-bit digitization.

The interstellar dispersion toward RX J0720.4–3125 is

unknown, but we can estimate it with the latest model of Galactic electron density (Cordes & Lazio 2002) which predicts a dispersion measure  $\text{DM} = 4 \text{ pc cm}^{-3}$  at  $d = 300 \text{ pc}$  or  $\text{DM} = 30 \text{ pc cm}^{-3}$  at  $d = 500 \text{ pc}$ . We therefore take  $\text{DM} = 100 \text{ pc cm}^{-3}$  as a conservative upper limit to the DM (the search was highly insensitive to DM anyway, given the long period of RX J0720.4–3125). Both datasets were de-dispersed with dispersion measures up to  $100 \text{ pc cm}^{-3}$  and searched for periodicities near the known X-ray period (Kaplan et al. 2002b; Zane et al. 2002) using standard folding and FFT-based techniques. No pulsar-like signals were detected.

Without a detection, we must estimate the limiting flux of a signal. While the search is insensitive to DM, the shape of the hypothetical pulse profile strongly affects the sensitivity. Assuming a pulse duty cycle of  $w = 1\%$ , our  $8\sigma$  detection limits are 0.2 mJy at 644 MHz and 0.02 mJy at 1374 MHz, and they scale approximately as

$$S_{\text{min}, 644 \text{ MHz}} = 2.0 \sqrt{\frac{w}{1-w}} \text{ mJy}$$

$$S_{\text{min}, 1374 \text{ MHz}} = 0.18 \sqrt{\frac{w}{1-w}} \text{ mJy}. \quad (4)$$

For signals with high  $w$  (i.e. few harmonics) the 1.4 GHz sensitivity is comparable to that of the VLA observations (§ 4.1), where the large bandwidth of the multibeam system compensates for its smaller area and shorter integration. However, for very narrow signals (where many harmonics are summed) the periodicity search is a factor of  $\sim 7$  deeper than the VLA observations.

## 5. DISCUSSION

### 5.1. The Spectrum

We have shown in § 2 that the optical/UV spectrum of RX J0720.4–3125 does not follow a pure Rayleigh-Jeans tail. It is possible that the emission (minus the contribution of the Rayleigh-Jeans tail of the X-ray spectrum) is entirely non-thermal in origin (like the Crab pulsar, where the non-thermal emission entirely overwhelms any thermal component). However, the slope of the spectrum,  $\alpha_\nu = 1.1$  is much steeper than that seen for other pulsars, whose spectral indices range from  $\alpha_\nu = 0.11$  for the Crab (Sollerman et al. 2000) to  $\alpha_\nu \sim -1$  for other sources (Zharikov et al. 2002, and references therein). In addition, the low spin-down power of RX J0720.4–3125 ( $\dot{E} < 2.4 \times 10^{31} \text{ ergs s}^{-1}$ ; Kaplan et al. 2002b) compared to sources like the Crab or even middle-aged radio pulsars means that there is no reason to expect this much non-thermal emission from RX J0720.4–3125.

Of the six other isolated neutron stars with good optical/UV data, there are three (all  $\lesssim 10^6 \text{ yr}$  old and within 500 pc) that show evidence for thermal optical emission: the pulsars PSR B0656+14 (Pavlov, Welty, & Córdoba 1997) and Geminga (Martin, Halpern, & Schiminovich 1998)<sup>9</sup>, and the nearby isolated neutron star RX J1856.5–3754 (van Kerkwijk & Kulkarni 2001b). [For the  $10^4$ -yr Vela pulsar, the optical emission (Mignani &

<sup>9</sup> Martin et al. (1998) find the PL+RJ model acceptable for Geminga, although a single non-thermal PL is also allowed. In addition, they require an absorption feature in the spectrum.

TABLE 7  
SUMMARY OF VLA OBSERVATIONS

Date (UT)	Frequency (GHz)	Exposure (sec)	Config.	Beam Size (asec)	RMS ( $\mu$ Jy)
1998-Feb-07	8.4	6720	D→A <sup>a</sup>	15'' × 5''.8	40
1999-Feb-18	1.4	4410	DnC	36'' × 32''	80
1999-Apr-19 <sup>b</sup>	1.4	7380	D	...	...

NOTE.—Observations all had  $2 \times 50$ -MHz bandwidths.

<sup>a</sup>Data were taken while switching from D configuration to A configuration.

<sup>b</sup>Processed with the 1999-Feb-18 observation.

Caraveo 2001) is dominated by the non-thermal component, but the X-ray spectrum contains thermal and non-thermal contributions (Pavlov et al. 2001.) Of these sources, RX J1856.5–3754 and PSR B0656+14 have thermal X-ray spectra too, like RX J0720.4–3125. We therefore believe that the optical/UV emission from RX J0720.4–3125 is mostly thermal in nature (i.e.  $\alpha_\nu = 2$ ), with the deviation from a Rayleigh-Jeans tail arising either due to a multiplicative opacity or to an added component. We address each of these models separately.

#### 5.1.1. One Component Model with Absorption

It is possible that the emission from RX J0720.4–3125 is entirely thermal, but that the underlying Rayleigh-Jeans tail is modified by a frequency-dependent absorption to give the observed spectrum. An opacity  $\kappa_\nu \propto \nu^{0.9}$  would give the correct result. However, this model is artificial, and is entirely contrary to what is seen with RX J1856.5–3754, PSR B0656+14, and the X-ray spectrum of RX J0720.4–3125 itself (§ 2.2.1). While we cannot reject this model based on our data alone, comparison with other sources makes it unlikely.

#### 5.1.2. Two Component Model

A simpler and more physically motivated model for the optical/UV spectrum of RX J0720.4–3125 is that the emission is composed of significant thermal emission plus a non-thermal PL (the PL+RJ model) similar to the spectra of PSR B0656+14 and Geminga. We have plotted brightness temperatures derived from model optical/UV spectra for these sources and RX J1856.5–3754 in Figure 9. The sources exhibit some variety in their spectra, ranging from purely thermal (RX J1856.5–3754) to largely non-thermal (e.g., PSR B0656+14). While RX J0720.4–3125 shows less non-thermal emission than PSR B0656+14 or Geminga, it is otherwise unremarkable.

The (extinction corrected)  $B$ -band luminosity of RX J0720.4–3125 is  $L_B = 6.5 \times 10^{27} d_{300}^2$  ergs s<sup>-1</sup>. If we separate the non-thermal component, we find  $L_{B,\text{non-th}} = 3.2 \times 10^{27} d_{300}^2$  ergs s<sup>-1</sup>. This compares well with the optical luminosities of similarly-aged pulsars given in Zharikov et al. (2002), which have  $27 \lesssim \log L_B \lesssim 28$ . As such, RX J0720.4–3125 fits in with the pulsar population despite its low rotational power ( $\dot{E}$ ). We note, though, that

all of the sources in Zharikov et al. (2002) with  $\tau \gtrsim 10^5$  yr have very similar values of  $L_B$ , despite values of  $\dot{E}$  that vary by about 3 orders of magnitude, and that the values of  $L_B$  show no apparent correlation with  $\dot{E}$ . So it appears that  $L_B$  is not simply related to  $\dot{E}$ , contrary to what is seen in the X-ray regime (Becker & Trümper 1997, see below). It may be, as suggested by Zharikov et al. (2002), that the efficiency of producing optical emission increases with time for  $\tau \gtrsim 10^4$  yr so that  $L_B$  remains relatively constant despite variations in  $\dot{E}$  (i.e.  $L_B = \eta(t)\dot{E}$ , where  $d\eta(t)/dt > 0$  and  $d\dot{E}/dt < 0$ ), or it may just be that the  $L_B$  is not directly coupled to  $\dot{E}$ . A final possibility is that the true distribution of  $L_B$  is closely tied to  $\dot{E}$  but that we only see the brightest sources in this distribution due to observational bias: a source with  $\log L_B = 26.5$  at 500 pc would

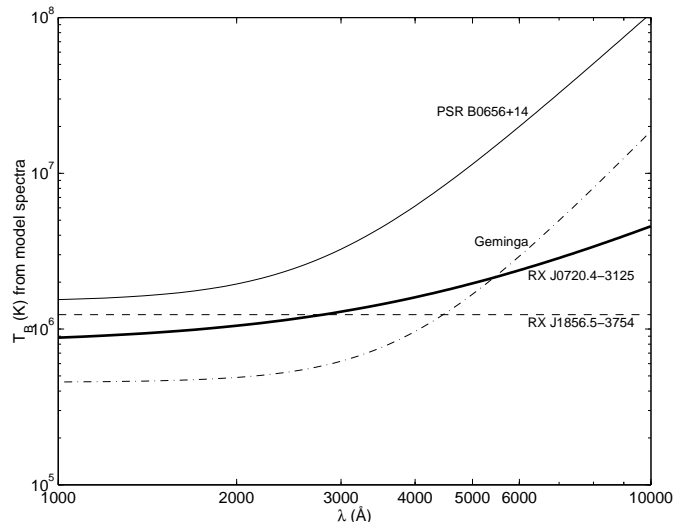


FIG. 9.— Brightness temperature  $T_B$  vs. wavelength for for RX J0720.4–3125 (solid line, this paper), RX J1856.5–3754 (dashed line, van Kerkwijk & Kulkarni 2001b), PSR B0656+14 (dotted line, Pavlov et al. 1997), and Geminga (dot-dashed line, Martin et al. 1998). The brightness temperature is defined as  $T_B(\lambda) \equiv F_\nu(\lambda)\lambda^2\Omega/2k$ , and the values were computed from model optical/UV spectra assuming a radius of 10 km and distances of 300 pc, 140 pc, 330 pc (Kaplan et al. 2002c; Walter & Lattimer 2002), and 160 pc (Caraveo et al. 1996), respectively. Deviations from a constant  $T_B$  indicate non-thermal emission.

have  $B \approx 31$  mag, below modern detection limits. Similarly, the very well studied RX J1856.5–3754 at  $\approx 140$  pc, the limit to non-thermal emission is  $\log L_B \lesssim 26.5$ . Therefore, any other source with  $\log L_B < 26.5$  could not be detected, and the true distribution of  $L_B$  may be poorly represented.

The slope of the non-thermal PL is  $\alpha_\nu \approx 0.3$ . This is consistent (within errors) with the slope of the optical PL for the Crab, and is not that far from the slope of the spectrum of PSR B0656+14 ( $\alpha_\nu = -0.45 \pm 0.26$ ; Koptsevich et al. 2001). The non-thermal spectra of neutron stars have been observed to follow roughly the same slope for over  $\sim 5$  orders of magnitude in energy (e.g., Koptsevich et al. 2001), suggesting a single underlying mechanism for the non-thermal optical and X-ray power-laws. Here, the non-thermal PL would contribute  $\sim 1\%$  of the flux of the blackbody in the LETG band and would therefore be difficult to observe:  $F(1 \text{ keV}) = (5_{-4}^{+25}) \times 10^{-13} \text{ ergs s}^{-1} \text{ cm}^{-2}$ . At higher energies ( $\gtrsim 2 \text{ keV}$ ) the non-thermal PL could contribute substantial X-ray flux (although the PL is highly uncertain at these energies; see Figure 4), flux that was not detected in the *Chandra* or *XMM* data. The *XMM* EPIC-pn data roughly give a flux of  $2 \times 10^{-14} \text{ ergs s}^{-1} \text{ cm}^{-2}$  at 1.5 keV, consistent with a blackbody and barely consistent with the extrapolated optical/UV power-law. So, for RX J0720.4–3125 the non-thermal spectrum is not likely to bridge the X-ray and optical regimes.

Becker & Trümper (1997) have found a rough relation between the spin-down power and the non-thermal X-ray emission of pulsars:  $L_{X,\text{non-th}} \sim 10^{-3} \dot{E}$  (with  $L_{X,\text{non-th}}$  in the *ROSAT* band of 0.1–2.4 keV). Applying this to RX J0720.4–3125 we would expect  $L_{X,\text{non-th}} \lesssim 10^{28} \text{ ergs s}^{-1}$ , or  $F_{X,\text{non-th}} \lesssim 10^{-15} \text{ ergs s}^{-1} \text{ cm}^{-2}$ . This is a factor of  $> 10^4$  less than the observed thermal X-ray flux in the same band, and a factor of  $10^2$  less than the extrapolated non-thermal emission. However, there is considerable uncertainty in both the relation of Becker & Trümper (1997) (see, e.g., Possenti et al. 2002) and in the extrapolation of the non-thermal PL to the X-ray regime, so the difference between  $F_{X,\text{non-th}}$  predicted from the spin-down and that predicted from the optical/UV spectrum may not be significant.

The thermal component in the optical/UV band is, like that of RX J1856.5–3754, above a simple extrapolation of the X-ray spectrum (for RX J1856.5–3754 it exceeds the X-rays by a factor of  $\sim 16$ ; van Kerkwijk & Kulkarni 2001b). This could just be a matter of temperature, though. For the sources PSR B0656+14 and PSR B1055–52, the X-ray spectrum is best-fit by a combination of a power-law and two blackbody components (Greiveldinger et al. 1996; Pavlov, Welty, & Córdoba 1997; Koptsevich et al. 2001; Marshall & Schulz 2002; Pavlov, Zavlin, & Sanwal 2002), where the smaller hot portion (presumably the polar cap) contributes the majority of flux in the traditional X-ray band but the larger cool portion (along with the non-thermal emission) gives rise to the optical/UV flux (Pavlov et al. 2002). In both cases, the blackbody components are all hot enough ( $\gtrsim 8 \times 10^5 \text{ K}$ ) to appear in the X-ray band, and are therefore well modeled.

For RX J1856.5–3754, which is closer in temperature to RX J0720.4–3125, Braje & Romani (2002) again ap-

pealed to a multitemperature surface, but here the second blackbody is not observed but only inferred (also see Walter & Lattimer 2002). It must be too cool for the X-ray band ( $T_{\text{cold}} \lesssim 5 \times 10^5 \text{ K}$ ), while still hot enough to appear as a power-law in the optical/UV band. While not very well constrained, this model gave reasonable results for RX J1856.5–3754, including a weak constraint on the radius, and is therefore valuable. We now apply this model to RX J0720.4–3125.

We see from Table 6 that a second (unconstrained) blackbody component does not appreciably change the X-ray fit. However, we can use the goodness-of-fit (given by  $\chi^2$ ) to constrain the combinations of  $T_{\text{cold}}$  and  $R_{\text{cold}}$  that are allowed. The flux of a Rayleigh-Jeans tail goes as  $F_\nu \propto R^2 T$ . We know that the X-ray blackbody has  $R_{\text{hot}} = 6.1 d_{300} \text{ km}$  and  $T_{\text{hot}} = 9.45 \times 10^5 \text{ K}$ , and since the thermal fit to the optical/UV data is a factor of 2.4 above the X-ray extrapolation, we find

$$T_{\text{cold}} = 2.4 \times 10^5 \left( \frac{R_{\text{cold},15}}{d_{300}} \right)^{-2} \text{ K}, \quad (5)$$

where the cold radius  $R_{\text{cold}} = 15 R_{\text{cold},15} \text{ km}$  has been taken to be the radius of the neutron star. Such a cool blackbody would not have been seen in the X-ray data (as shown by the large uncertainties on  $R_{\text{cold}}$  in Tab. 6), but we can constrain  $T_{\text{cold}}$  to be  $\approx (3.5\text{--}5.0) \times 10^5 \text{ K}$ , or  $R_{\text{cold}} \approx (11\text{--}13) d_{300} \text{ km}$  (at roughly 90% confidence). This is similar to the temperature of the cold component found for RX J1856.5–3754 (Braje & Romani 2002) — not surprising since in both cases the cold component was forced to give a Rayleigh-Jeans tail in the optical while not giving significant contribution in the soft X-rays — and the size agrees well with estimates for the radius of a neutron star (Lattimer & Prakash 2000).

Cropper et al. (2001) model the phase-dependent hardness ratio of RX J0720.4–3125 in *XMM* data, and find that it is consistent with a polar-cap model for a large range of cap sizes with angular radii of  $10\text{--}50^\circ$ . This agrees quite well with our findings ( $R_{\text{cold}} = 15 d_{300} \text{ km}$  corresponds to an angular radius of  $\approx 25^\circ$ ).

Taken together, these observations show that a RJ+PL model for the optical/UV spectrum of RX J0720.4–3125 makes it entirely consistent with being an off-beam radio pulsar, one that likely has a cooler blackbody component in the extreme UV.

### 5.1.3. Constraints on the Magnetic Field

We find no significant absorption features in the pulse-averaged or pulse-phased spectra over the 0.15–0.80 keV band (§ 3). Thus, following Marshall & Schulz (2002) and Paerels et al. (2001), we can rule out electron and proton cyclotron resonance lines in this range. Paerels et al. (2001) already rule out the range  $0.03 < B_{12} < 0.2$  and  $50 < B_{12} < 200$ , where  $B_{12} = B/(10^{12} \text{ G})$ . By extending the spectrum down to 0.15 keV, we extend the lower limits of the excluded ranges of magnetic fields to  $B_{12} = 0.015$  and  $B_{12} = 25$ , though the lower limits could increase if the bulk of the emission comes from the equatorial zone, where the magnetic field is  $\sim 50\%$  of the polar value, or if the absorbing plasma is far off the neutron surface. We can also use the lack of features in the spectrum to exclude hydrogen atmospheres for a range of magnetic field strengths. Again following Paerels et al. (2001), we can exclude the

range  $B_{12} > 15$ . The excluded ranges of  $B$  agree with the finding that RX J0720.4–3125 is not a magnetar (Kaplan et al. 2002b), but otherwise the  $B$  is consistent with either of the models discussed in Kaplan et al. (2002b, see also § 5.2), namely that have  $B_{12} \approx 1$ –10.

### 5.2. Radio Luminosity

At a distance of  $300d_{300}$  pc, we limit the 1.4 GHz radio luminosity of RX J0720.4–3125 to  $< 3 \times 10^{25} d_{300}^2$  ergs s<sup>-1</sup> ( $L_{\text{rad}} \equiv 4\pi d^2 F$ ), or following the radio pulsar convention  $L'_{\text{rad}} < 0.02$  mJy kpc<sup>2</sup> ( $L'_{\text{rad}} \equiv F d^2$ ). This is significantly below what is expected of radio pulsars with parameters ( $P$  and  $\dot{P}$ ) similar to those of RX J0720.4–3125. For instance, the two high- $B$  radio pulsars discovered by Camilo et al. (2000) have  $L_{\text{rad}} \sim 5 \times 10^{26}$  ergs s<sup>-1</sup>, while the 8-s 10<sup>12</sup>-G pulsar PSR J2144–3944 has  $L_{\text{rad}} \sim 10^{30}$  ergs s<sup>-1</sup> (Young et al. 1999). Similarly, the radio luminosity model of Arzoumanian, Chernoff, & Cordes (2002) predicts luminosities of  $10^{27-28}$  ergs s<sup>-1</sup>, depending on the value of  $\dot{P}$ . So we can see that RX J0720.4–3125, if it has any radio emission, must be beamed away from the Earth.

If RX J0720.4–3125 is like PSR J2144–3944, then we might expect a similarly narrow radio beam of  $w \approx 0.6\%$ , a beam width that agrees well with the extrapolation of Rankin (1993). RX J0720.4–3125 may however be more similar to the 10<sup>13</sup> G radio pulsar PSR J1814–1744 (Camilo et al. 2000), which has a significantly wider beam ( $w \approx 3\%$ ). In either case, we can expect that the radio beam subtends a small solid angle, making the lack of radio emission quite credible. For such beams, our upper limits to the radio luminosity *decrease*, as the limit from the Parkes data for a source with pulse width of  $w = 0.6$ –3% at 1.4 GHz is  $L'_{\text{rad}} \approx 0.002$  mJy kpc<sup>2</sup>. Even the imaging (VLA) limit is quite faint, about a factor of 3 fainter than the limit for Geminga (Seiradakis 1992), and a factor of  $\sim 30$  below that of PSR J0205+6449 in 3C 58 (Camilo et al. 2002), but the implied limit for a narrow pulse width is far below that of all radio pulsars younger than 10<sup>6</sup> yr (Motch 2001).

With such small beams, the radio-quiet population of sources like RX J0720.4–3125 could potentially be very large, up to a hundred times the radio-loud population (assuming a sharp cutoff in the radio beam). While likely invisible to radio observations, such sources are of course bright X-ray emitters, and would be visible to  $\sim 5$  kpc in a 30 ksec *XMM* observation. The total numbers of such sources (either radio-loud or -quiet) are small, making statistics uncertain, but there could be cooling radio-quiet neutron stars in as much as 1% of *XMM* observations. However, these sources would be all but impossible to confirm, as there would be few X-ray photons for spectral fitting or pulsation searches, and the optical/UV counterpart would be extremely faint.

## 6. CONCLUSIONS

We have shown, through a joint analysis of radio, optical, and X-ray data, that the spectrum of the isolated neutron star RX J0720.4–3125 cannot be fit by a single blackbody model. While statistically we cannot rule out a model with a single power-law in the optical/UV domain and an X-ray blackbody, from a more general perspective

we believe that the best-fit model is one with three components: a hot ( $\sim 9 \times 10^5$  K) blackbody on the polar cap, a cool ( $\sim 4 \times 10^5$  K) blackbody over the whole surface, and a weak non-thermal power-law in the optical/UV. This is very similar to the spectra of middle aged radio pulsars such as PSR B0656+14 and PSR B1055–52, an observation that supports the identification of RX J0720.4–3125 with an off-beam radio pulsar.

RX J0720.4–3125 appears extremely similar to the very nearby RX J1856.5–3754, perhaps with orientation being the only difference between them (Braje & Romani 2002). We believe it likely that non-thermal emission and/or pulsations will be detected eventually for RX J1856.5–3754, as suggested by Braje & Romani (2002). Both sources seem to have spectra primarily composed of featureless blackbodies. If we can develop a full understanding of such spectra to properly relate the blackbody radii (such as that given here) to the true radii, these sources will be ideal targets for the determination of the equation-of-state.

In the near future, we will obtain *HST* astrometry allowing us to determine the distance and velocity of RX J0720.4–3125, as well as H $\alpha$  imaging to search for bow-shock nebulae (e.g., van Kerkwijk & Kulkarni 2001a) that will place significant constraints on alternate models such as accretion. In the off-beam pulsar model, these data may limit the luminosity of any particle wind from RX J0720.4–3125, and will reduce uncertainty in the EOS by determining the conversion from solid angle to radius.

We thank the anonymous referee for valuable comments. D. L. K. is supported by the Fannie and John Hertz Foundation and S. R. K. by NSF and NASA. M. H. v. K. is supported by a fellowship from the Royal Netherlands Academy of Arts and Sciences. H. L. M. was supported under NASA contract SAO SV1-61010. DLK also thanks *Chandra* grant GO0-1024X for additional support. Data presented herein were based on observations made with the NASA/ESA Hubble Space Telescope, obtained at the Space Telescope Science Institute, which is operated by the Association of Universities for Research in Astronomy, Inc., under NASA contract NAS 5-26555. The National Radio Astronomy Observatory is a facility of the National Science Foundation operated under cooperative agreement by Associated Universities, Inc. Data presented herein were also obtained at the W. M. Keck Observatory, which is operated as a scientific partnership among the California Institute of Technology, the University of California, and the National Aeronautics and Space Administration. The Guide Star Catalog-II is a joint project of the Space Telescope Science Institute and the Osservatorio Astronomico di Torino.

## REFERENCES

- Alpar, M. A. 2001, ApJ, 554, 1245
- Arzoumanian, Z., Chernoff, D. F., & Cordes, J. M. 2002, ApJ, 568, 289
- Becker, W. & Trümper, J. 1997, A&A, 326, 682
- Bessell, M. S., Castelli, F., & Plez, B. 1998, A&A, 333, 231
- Braje, T. M. & Romani, R. W. 2002, ApJ, 580, 1043
- Camilo, F., Kaspi, V. M., Lyne, A. G., Manchester, R. N., Bell, J. F., D’Amico, N., McKay, N. P. F., & Crawford, F. 2000, ApJ, 541, 367

- Camilo, F., et al. 2002, *ApJ*, 571, L41
- Caraveo, P. A., Bignami, G. F., Mignani, R., & Taff, L. G. 1996, *ApJ*, 461, L91
- Cardelli, J. A., Clayton, G. C., & Mathis, J. S. 1989, *ApJ*, 345, 245
- Condon, J. J., Cotton, W. D., Greisen, E. W., Yin, Q. F., Perley, R. A., Taylor, G. B., & Broderick, J. J. 1998, *AJ*, 115, 1693
- Cordes, J. M. & Lazio, T. J. W. 2002, *astro-ph/0207156*
- Cropper, M., Zane, S., Ramsay, G., Haberl, F., & Motch, C. 2001, *A&A*, 365, L302
- Drake, J. J., et al. 2002, *ApJ*, 572, 996
- Fruchter, A. S. & Hook, R. N. 2002, *PASP*, 114, 144
- Greiveldinger, C., et al. 1996, *ApJ*, 465, L35
- Haberl, F., Motch, C., Buckley, D. A. H., Zickgraf, F.-J., & Pietsch, W. 1997, *A&A*, 326, 662
- Kaplan, D. L., Kulkarni, S. R., & van Kerkwijk, M. H. 2002a, *ApJ*, 579, L29
- Kaplan, D. L., Kulkarni, S. R., van Kerkwijk, M. H., & Marshall, H. L. 2002b, *ApJ*, 570, L79
- Kaplan, D. L., van Kerkwijk, M. H., & Anderson, J. 2002c, *ApJ*, 571, 447
- Konenkov, D. Y. & Popov, S. B. 1997, *Pis'ma Astron. Zh.*, 23, 569
- Koptsevich, A. B., Pavlov, G. G., Zharikov, S. V., Sokolov, V. V., Shibanov, Y. A., & Kurt, V. G. 2001, *A&A*, 370, 1004
- Kulkarni, S. R. & van Kerkwijk, M. H. 1998, *ApJ*, 507, L49
- Lattimer, J. M. & Prakash, M. 2000, *Phys. Rep.*, 333, 121
- Lyne, A. G., et al. 2000, *MNRAS*, 312, 698
- Marshall, H. L., Edelson, R. A., Vaughan, S., Malkan, M., O'Brien, P., & Warwick, R. 2002, *ApJ*
- Marshall, H. L. & Schulz, N. S. 2002, *ApJ*, 574, 377
- Martin, C., Halpern, J. P., & Schiminovich, D. 1998, *ApJ*, 494, L211
- Mignani, R. P. & Caraveo, P. A. 2001, *A&A*, 376, 213
- Motch, C. 2001, in *AIP Conf. Proc.* 599: X-ray Astronomy: Stellar Endpoints, AGN, and the Diffuse X-ray Background, 244 (*astro-ph/0008485*)
- Motch, C. & Haberl, F. 1998, *A&A*, 333, L59
- O'Donnell, J. E. 1994, *ApJ*, 422, 158
- Oke, J. B., et al. 1995, *PASP*, 107, 375
- Paerels, F., et al. 2001, *A&A*, 365, L298
- Pavlov, G. G., Welty, A. D., & Córdoba, F. A. 1997, *ApJ*, 489, L75
- Pavlov, G. G., Zavlin, V. E., & Sanwal, D. 2002, *astro-ph/0206024*
- Pavlov, G. G., Zavlin, V. E., Sanwal, D., Burwitz, V., & Garmire, G. P. 2001, *ApJ*, 552, L129
- Perna, R., Hernquist, L., & Narayan, R. 2000, *ApJ*, 541, 344
- Pons, J. A., Walter, F. M., Lattimer, J. M., Prakash, M., Neuhäuser, R., & An, P. 2002, *ApJ*, 564, 981
- Possenti, A., Cerutti, R., Colpi, M., & Mereghetti, S. 2002, *A&A*, 387, 993
- Predehl, P. & Schmitt, J. H. M. M. 1995, *A&A*, 293, 889
- Press, W. H., Teukolsky, S. A., Vetterling, W. T., & Flannery, B. P. 1992, *Numerical recipes in C. The art of scientific computing* (Cambridge: University Press, —c1992, 2nd ed.)
- Rankin, J. M. 1993, *ApJ*, 405, 285
- Romani, R. W. 1987, *ApJ*, 313, 718
- Seiradakis, J. H. 1992, *IAU Circ.*, 5532, 1
- Sollerman, J., Lundqvist, P., Lindler, D., Chevalier, R. A., Fransson, C., Gull, T. R., Pun, C. S. J., & Sonneborn, G. 2000, *ApJ*, 537, 861
- Stys, D. J., Walborn, N. R., Busko, I., Goudfrooij, P., Proffitt, C., & Sahu, K. 2002, *American Astronomical Society Meeting*, 200, 0
- Treves, A., Turolla, R., Zane, S., & Colpi, M. 2000, *PASP*, 112, 297
- van Kerkwijk, M. H. & Kulkarni, S. R. 2001a, *A&A*, 380, 221
- . 2001b, *A&A*, 378, 986
- Walter, F. M. & Lattimer, J. M. 2002, *ApJ*, 576, L145
- Wang, J. C. L. 1997, *ApJ*, 486, L119
- Young, M. D., Manchester, R. N., & Johnston, S. 1999, *Nature*, 400, 848
- Zane, S., Haberl, F., Cropper, M., Zavlin, V. E., Lumb, D., Sembay, S., & Motch, C. 2002, *MNRAS*, 334, 345
- Zharikov, S. V., et al. 2002, *A&A*, 394, 633